Research Article | Vol. 32, No. 22 / 21 Oct 2024 / Optics Express 39192
Optics EXPRESS

X-ray image reconstruction for continuous acquisitions with a generalized motion model

Ben Huyge,[1,2,*] Jens Renders,[1,2] Joaquim G. Sanctorum,[1,2] Jan De Beenhouwer,[1,2] and Jan Sijbers[1,2]

[1]imec - Vision Lab, Dept. of Physics, University of Antwerp, Universiteitsplein 1, 2610 Antwerp, Belgium
[2]DynXLab: Center for 4D Quantitative X-ray Imaging and Analysis, Universiteitsplein 1, 2610 Antwerp, Belgium
[*]ben.huyge@uantwerpen.be

Abstract: Continuous X-ray imaging is known to reduce mechanical vibrations and scan time compared to a step-and-shoot acquisition approach. However, motion during X-ray exposure leads to blurred projections and consequently to loss of spatial resolution and contrast in conventionally reconstructed images. Recent works that aim to reduce continuous motion blur focus only on rotational motion and often include linearization approximations, while many applications would benefit from a more generalized continuous acquisition strategy. In this paper, we propose a dedicated reconstruction technique for rotational, translational, and roto-translational motion, without requiring a linearization approximation. Through simulations and real experiments, we show that motion blur artifacts caused by roto-translational continuous scanning are substantially reduced, allowing for faster scanning while retaining image quality.

1. Introduction

X-ray computed tomography (XCT) is a well established technique to non-destructively inspect the internal structure of materials. Conventionally, an XCT scan is operated with a step-and-shoot acquisition scheme, where the object remains motionless during the acquisition of a single X-ray projection, after which the object is rotated to a new position [1]. Reconstruction algorithms for a step-and-shoot acquisition scheme assume a completely motionless object and stabilized imaging set-up while each projection is acquired. A major disadvantage of step-and-shoot imaging is the time required to complete a scan, which is significantly longer than a scan with a continuous acquisition scheme [2]. The scan is interrupted each time the object is repositioned. This results in a limitation on the throughput that is achievable by the scanner and is therefore undesirable for industrial applications in which a large number of objects must be scanned in a short time span. Additionally, for imaging dynamic processes, the relatively long scanning time of a step-and-shoot scan hinders the scanning of fast dynamic processes, limiting the temporal resolution. When imaging dynamic processes, dedicated reconstruction techniques are required to take the object motion into account, such as gating if the motion is periodic [3] or general motion compensation techniques [4]. Moreover, a step-and-shoot approach requires numerous short accelerations and decelerations, which may cause small, unwanted object motions due to inertia of the object or gantry.

In continuous acquisition, the object rotates uninterruptedly while images are acquired. Such an acquisition strategy considerably reduces the scanning time because the scan is not halted each time the object is repositioned. Continuous acquisition is especially useful in applications such as high-throughput XCT and in-situ XCT [5]. In high-throughput XCT, the manufactured objects are preferentially scanned at the same speed at which they are produced, to ensure an efficient production process. A higher throughput can be achieved by placing the object on a

#531999 https://doi.org/10.1364/OE.531999
Journal © 2024 Received 4 Jun 2024; revised 2 Aug 2024; accepted 4 Aug 2024; published 14 Oct 2024

Optics EXPRESS

conveyor belt, so that the object moves through the X-ray beam (with or without simultaneous rotation). This can be realized with different object and gantry configurations, e.g. with a static source [6], multiple static sources [7], a single rotating source [8,9] or a translating source [10]. In in-situ XCT, a dynamic process is imaged continuously, providing a time series of 3D images. Here, the scanning speed is vital as it determines the temporal resolution at which the process can be captured [11]. Unfortunately, while the increased scanning speed of a continuous acquisition scheme is desirable for many applications, motion during X-ray exposure leads to artifacts in the reconstructed image because of signal integration in the detector pixels, causing a degradation of image quality [12,13].

To alleviate blurring artifacts in the reconstructed image caused by continuous rotation during X-ray exposure, a dedicated reconstruction technique denoted Algebraic Reconstruction Technique with angular Integration Concept (ARTIC) was proposed [14]. ARTIC accounts for angular integration in the reconstruction and has shown to reduce blur. However, since ARTIC relies on algebraic reconstruction, approximations were introduced to linearize the forward model. Chen et al. proposed an alternative method for continuous scanning in which the motion-blurred sinogram is deconvolved to obtain a quasi-static sinogram that serves as input for a conventional reconstruction algorithm [15]. However, rotational symmetry and a constant rotation speed are assumed. More recently, a method using machine learning was developed by Zhang et al., where first the motion blurred sinogram is reconstructed with a filtered-back-projection, resulting in an image with motion artifacts [16]. This image is then given as input to a residual-in-residual-dense-block network that aims to reduce the motion artifacts. However, this implies that the network highly depends on the initial reconstruction of the motion blurred projections used for training the network. In another recent method, the acquisition process is encoded using a shutter placed in front of the detector to modulate the X-ray flux [17]. During integration, the measured signal is encoded by opening and closing the shutter multiple times according to a chosen pattern, called a binary code. The framework then uses this code in the reconstruction scheme to reduce the blurring artifacts. While motion blur is reduced, this technique requires additional hardware in the form of a shutter that can open and close at a high frequency, which may not be readily available.

In summary, the methods that have been proposed to alleviate motion blur in continuous X-ray scanning assume rotational motion and/or rely on approximate (linearized) imaging models. However, many applications require more complex motion during acquisition, inhibiting the use of existing methods. Hence, there is a need for a reconstruction method that incorporates both rotational and translational motion in a flexible way into the reconstruction algorithm to reduce motion artifacts in the reconstructed images.

In this paper, we propose a reconstruction method that models the motion during X-ray exposure called Reconstruction Algorithm for Continuous Exposure (RACE). Compared to ARTIC, RACE does not require a linearization approximation of the forward model. Moreover, it allows for scan geometries with combined rotation and translation, and hence scan geometries that are suited for conveyor belt scanning. We show that RACE largely removes the artifacts caused by rotational motion blur in the projections, resulting in a higher reconstruction quality compared to ARTIC. Also, for roto-translational motion, RACE results in a considerably higher reconstruction quality, even for a small number of projections.

2. Methods

In a step-and-shoot acquisition scheme, the object remains stationary during X-ray exposure. Consequently, the measured intensity I of the n^{th} projection at a position r on the detector and at a certain rotation angle θ_n can be expressed via the Beer-Lambert law [18],

$$I_n(r) = I_0 \exp\left(-\int_{L_{r,\theta_n}} \mu(x,y)ds\right), \tag{1}$$

Optics EXPRESS

where I_0 is the intensity measured without an object and the line integral integrates over the path of the monochromatic X-rays L_{r,θ_n}. The attenuation coefficient is given by $\mu(x, y)$ as a function of the coordinates $(x, y) = (s\sin\theta + r\cos\theta, -s\cos\theta + r\sin\theta)$ for a parallel beam geometry. This parametrization can be adapted to accomodate for a fan or cone beam geometry if necessary [19]. In algebraic reconstruction techniques, Eq. (1) is discretized to a system of linear equations that can be solved to obtain the reconstructed image.

In continuous acquisition the object moves relative to the X-ray beam during exposure, so that the path of the X-ray through the object can not be described as a single straight line and Eq. (1) becomes invalid. The measured intensity is now integrated over a time interval Δt, equal to the exposure time of a single frame. In case of uniform circular motion, Eq. (1) can be adapted to include the intensity integration over the angular interval $\theta_{\text{int}} = \omega\Delta t$, with ω the rotation velocity,

$$I_n(r) = \frac{I_0}{\theta_{\text{int}}} \int_{\alpha=\theta_n}^{\theta_n+\theta_{\text{int}}} \exp\left(-\int_{L_{r,\alpha}} \mu(x, y)ds\right) d\alpha. \tag{2}$$

Equaton (2) is used in ARTIC to reduce rotational motion blur by discretizing the integral over the angular interval and by applying a linearization approximation so an algebraic reconstruction technique can be used [14].

In RACE, this linear approximation is avoided by instead modelling the motion during X-ray exposure by a blurring operator that acts on a set of subsampled projections, which are distributed over the angular interval. Each angular interval θ_{int} is subsampled by a subsampling factor M into smaller intervals of equal size, assuming a constant rotation speed. M should be large enough so the angular integration over θ_{int}/M is well approximated by the finite sum over M, but a larger M also requires more computation time and memory. To estimate a value for M, we state that the arc length traversed by the object while rotating over θ_{int}, must be smaller than the voxel size w [16]. The arc length is given by $a\theta_{\text{int}}$, where a is the maximal radius of the object. We approximate that radius by half the size of the reconstruction grid, given by $kw/2$, with k the number of voxel columns. A lower bound for M is then calculated by,

$$\frac{\frac{kw}{2}\theta_{\text{int}}}{M} < w \Leftrightarrow M > \frac{k\theta_{\text{int}}}{2}. \tag{3}$$

We use the smallest integer for M that satisfies Eq. (3) to subsample the angular interval.

Moreover, the subsampling in RACE can easily be adapted to include translational motion, for scans where rotation is combined with translation (e.g. conveyor belt and helical scanning). For a translational motion during the exposure time Δt, the interval over which the intensity is integrated is given by $r_{\text{int}} = v\Delta t$, with v the translation velocity. Eq. (2), can then be further adapted to include the integration over the translation,

$$I_n(r) = \frac{I_0}{\theta_{\text{int}} r_{\text{int}}} \int_{\xi=r}^{r+r_{\text{int}}} \int_{\alpha=\theta_n}^{\theta_n+\theta_{\text{int}}} \exp\left(-\int_{L_{\xi,\alpha}} \mu(x, y)ds\right) d\alpha d\xi. \tag{4}$$

In general, the subsampling scheme can be chosen to accommodate for various types of motion during continuous acquisition, which makes RACE widely applicable. Figure 1 schematically shows three different examples of subsampling schemes: a purely rotational motion (Fig. 1(a)), a purely translational motion (Fig. 1(b)) and a combined motion (Fig. 1(c)) during acquisition.

In practice, the first step in RACE is to subsample the motion interval over which the intensity is integrated, resulting in a set of M subsampled projections for each of the N effectively measured (motion blurred) projections during the scan. The complete set of $M \times N$ projections, denoted $\boldsymbol{p}_{sub}$, is then blurred by an operator B that averages the projections in separate groups of M via

$$B(\boldsymbol{p}_{sub}) = -\log(\text{avg}(\exp(-\boldsymbol{p}_{sub}))), \tag{5}$$

where avg(.) calculates the average over every disjunct, but adjacent, group of M subsampled projections (indicated by a separate color in Fig. 1). This averaging is the discrete equivalent

Optics EXPRESS

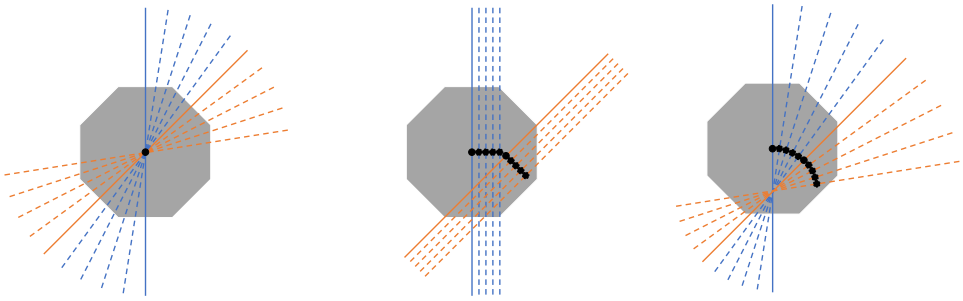

(a) Rotational motion (b) Translational motion (c) Combined motion

Fig. 1. A subsampling scheme for different types of motion during acquisition. The full lines represent the starting position of the integrated projections. The dotted lines are the additional subsampled projections to model the motion during X-ray exposure for a purely rotational motion (a), a purely translational motion (b) and a combined motion (c).

of the integrals over the translation and rotation in Eq. (4). Before averaging, the log-corrected projections are first converted to intensities using the exponent, to model the integration of intensity occurring in the detector pixels. Afterwards, the averaged intensities are converted back to log-corrected projection data.

Finally, RACE uses the objective function,

$$f(\boldsymbol{x}) = \frac{1}{2}||B(\boldsymbol{W}_s\boldsymbol{x}) - \boldsymbol{p}||_2^2, \tag{6}$$

where $\boldsymbol{p}$ is the vector of N continuously acquired motion blurred projections, $\boldsymbol{x}$ is the unknown image and $\boldsymbol{W}_s$ is the subsampled system matrix. This matrix contains the weights of each ray going through a voxel for the complete set of $M \times N$ subsampled projections, so that $\boldsymbol{p}_{sub} = \boldsymbol{W}_s\boldsymbol{x}$. The unknown image $\boldsymbol{x}$ is calculated from Eq. (6) by minimizing the projection distance between the continuously acquired projections and the blurred forward projections by a minimization method of choice. Here, we use gradient descent with a Barzilai-Borwein step size to minimize the objective function in Eq. (6) [20].

RACE will be compared to ARTIC and a conventional reconstruction that does not take motion during continuous acquisition into account. For the conventional reconstruction technique (denoted with BBLS), the objective function,

$$f(\boldsymbol{x}) = \frac{1}{2}||\boldsymbol{W}\boldsymbol{x} - \boldsymbol{p}||_2^2, \tag{7}$$

is minimized with gradient descent with a Barzilai-Borwein step size, to obtain the unknown image $\boldsymbol{x}$. The matrix $\boldsymbol{W}$ is the conventional non-subsampled projection matrix. To provide a fair comparison, the linear system of ARTIC is also solved with gradient descent with a Barzilai-Borwein step size, instead of SIRT originally [14]. A non-negativity constraint is applied to all reconstructions.

3. Experiments

To quantify the performance of RACE in comparison to the state-of-the-art, simulations (Section 3.1) and real experiments (Section 3.2) were set up.

3.1. Simulations

The simulations were performed with the ASTRA Toolbox, a high-performance GPU accelerated and flexible simulation framework for 2D and 3D X-ray tomography [21]. In the simulations,

Optics EXPRESS

the scanning geometry was defined with a source-to-object distance of 0.50 m and an object-to-detector distance of 0.25 m, resulting in a magnification factor of 1.5. The source emitted a fan beam with an opening angle of approximately 14° and the detector consisted of a row of 1250 pixels, where each pixel had a width of 150 µm. The phantom had dimensions of 1400×1400 voxels, and the reconstruction grid comprised of 700×700 voxels, with each voxel measuring 100 µm in width. Note that the images were reconstructed on a different grid to avoid an inverse crime. The projections were equally distributed over a range of 180° plus the fan angle to ensure completeness of the dataset [22]. The number of projection angles N varied depending on the simulation. The phantom used for the simulations is shown in Fig. 2.

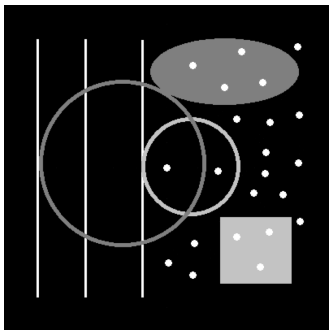

Fig. 2. The phantom from which the motion blurred projections are simulated.

To simulate N motion blurred projections, a subsampling factor of $M = 1000$ was used to generate a set of $M \times N$ static projections. Next, from this set of simulated step-and-shoot projections, N motion blurred projections were obtained by averaging disjoint, yet adjacent, sets of M consecutive projections. The subsampling factor to generate the motion blurred projections was chosen to be at least an order of magnitude higher than the subsampling factors used in the reconstruction of the data, so that this approach is still a valid approximation for a continuous acquisition.

3.1.1. Continuous acquisition with rotational motion

To compare RACE to the state-of-the-art technique ARTIC, simulations were performed in which there was only rotational motion of the object during continuous acquisition, as this is a limitation of ARTIC. The RACE and ARTIC reconstructions are compared for different numbers of projections and noise levels.

In a first experiment, $N = 40$ noiseless motion blurred projections were simulated from the phantom shown in Fig. 2, equally distributed over 180° plus the fan angle. The projections were reconstructed with 2000 BBLS iterations, without taking the continuous acquisition into account. Then, the phantom was reconstructed with 2000 ARTIC and RACE iterations. For ARTIC and RACE, a subsampling factor of $M = 30$ was used, calculated with Eq. (3). For the BBLS reconstruction, the projections were given an angle offset of half the blurring angle (approximately 2.4°) so that the image was reconstructed according to the same orientation as the ARTIC and RACE reconstructions. ARTIC and RACE automatically correct for this effect and do not require an additional angular offset. Then, the simulation was repeated for $N = 20$ and $N = 10$ equally distributed projections, simulating fast continuous scans. The corresponding subsampling factors were calculated with Eq. (3), resulting in subsampling factors of $M = 120$ and $M = 60$, respectively.

In the second experiment, the phantom from Fig. 2 was reconstructed with RACE and ARTIC from $N = 40$ equally distributed motion blurred projections, with different amounts of Poisson

Optics EXPRESS

noise added. The expected number of photon detections per pixel were $I_0 = 10^4$ and $I_0 = 10^5$. One of the properties of the Poisson distribution is that the expected value is also equal to the variance, meaning that the signal-to-noise-ratio is given by $\sqrt{I_0}$ [23].

3.1.2. Continuous acquisition with both rotational and translational motion

To evaluate the performance of RACE for roto-translational motion, simulations were performed where the phantom from Fig. 2 was translated orthogonal to the optical axis, resulting in a left to right shift in the projections, in combination with rotational motion. RACE is compared with ARTIC by applying the roto-translational subsampling scheme to the ARTIC model, although originally the model of ARTIC did not include translational motion. Therefore, we denote this method as ARTIC+.

First, three sets of motion blurred projections with $N = 10$, $N = 20$ and $N = 40$ projections, equally distributed over a range of 180° plus the fan angle, were simulated from the phantom shown in Fig. 2. No noise was added to the projections. These three datasets represent a fast continuous scan, in which only a limited amount of data can be captured. In addition to the rotational motion, a translational motion was added orthogonal to the optical axis. The phantom was translated with a distance of 0.4 mm per projection, corresponding to a shift of 4 pixels on the detector, per projection.

After simulating the three datasets, each one was first reconstructed with 2000 BBLS iterations, where the continuous motion of the object during acquisition was disregarded. For the BBLS reconstruction, an angle offset of half the blurring angle and a translation offset of half the shifted distance were added so that the reconstructed image is oriented and positioned the same way as the ARTIC+ and RACE reconstruction. This does not influence the blurring artifacts, but acts as a repositioning of the reconstruction so a proper comparison can be made. Then, RACE and ARTIC+ were used to reconstruct the phantom from the same set of motion blurred projections. For $N = 10$, $N = 20$ and $N = 40$ equally distributed projections, the amount of rotational blur was approximately 19.4°, 9.7° and 4.9°, respectively. The corresponding subsampling factors used in RACE and ARTIC+ were $M = 120$, $M = 60$ and $M = 30$, as determined via Eq. (3).

3.2. Real measurements

Real experimental data was measured with the FleXCT scanner, available at the DynXLab core facility [24,25]. This scanner has 10 degrees of freedom, enabling simultaneous object rotation and translation during exposure. The object in Fig. 3 was scanned with a tube voltage of 80 kV. The source to object distance was 500 mm and the source to detector distance was 750 mm, resulting in a magnification factor of 1.5. The pixel width of the detector is 150 μm and the acquired images have a dimension of 456×2856 pixels. To speed up the reconstruction and limit the memory requirement, only the central slice of the object was reconstructed. The reconstruction grid measured 1200×1200 voxels, with a voxel size of 100 μm.

First, a continuous scan was performed with 3600 projections covering a 360° range, in which the object did not translate. The object had a rotation speed of approximately 4° s^{-1} and the exposure time for one projection was 25 ms, resulting in a rotational motion blur of 0.1° per projection. This amount is negligible because the arc length traversed by the object during the exposure time is smaller than the voxel width. Therefore, this scan will serve as a reference to compare to the scan with larger motion blurring. The reference scan was reconstructed with 200 BBLS iterations.

Secondly, a scan with rotational and translational motion blur was performed. The rotation speed of the object was approximately 5 ° s^{-1} and the translation speed was 1.6 mm s^{-1}. The exposure time for one projection was 200 ms, resulting in a rotational blur of 1° and a translational blur of 0.48 mm per projection, equal to a shift of approximately 3 pixels on the detector. In

Optics EXPRESS

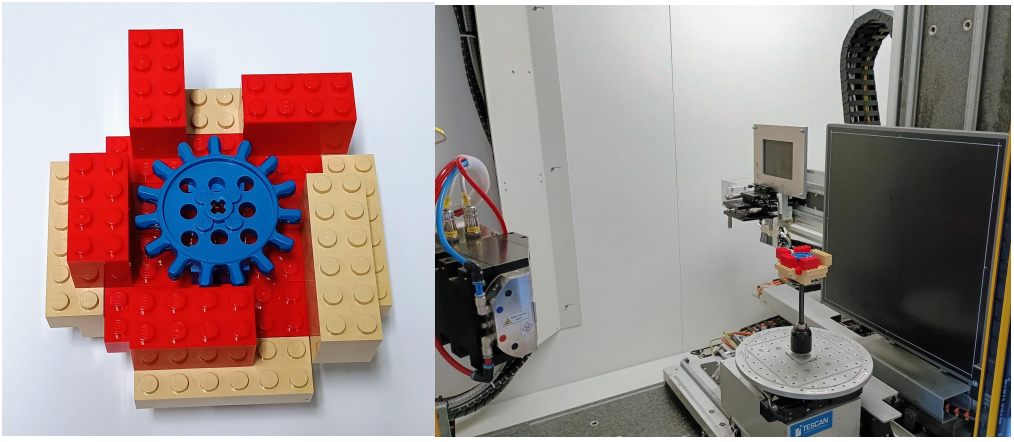

(a) Top view of the scanned object (b) The object in the FleXCT scanner

Fig. 3. An image of the scanned object (a) and the object positioned in the FleXCT scanner (b).

total, $N = 360$ projections were acquired over an angular range of 360° and a translation range of 172.8 mm projected on the detector plane.

To investigate higher amounts of rotational and translation blur, the intensities of adjacent projections were averaged together instead of measuring new data. With this approach, a dataset was generated with 2° and 4° of rotational blur per projection, and a translational blur of 0.96 mm and 1.92 mm, respectively.

The motion blurred projections were first reconstructed with BBLS, for which an offset of half the blurring angle and half the translated distance during exposure was added to correct the positioning of the reconstructed image. Then, the projections were reconstructed with ARTIC+ and RACE. To estimate the amount of iterations needed, the normalized mean squared error (NMSE) is calculated between the reference reconstruction and the RACE reconstruction by dividing the mean squared error by the variance of the reference reconstruction. The iteration was continued until the NMSE started to increase. For the dataset with 1°, 2° and 4° of rotational blurring, the iterations were 60, 70 and 108, respectively. For the ARTIC+ and RACE reconstruction of the three datasets, the subsampling factor determined with Eq. (3) was $M = 11$, $M = 22$ and $M = 44$, respectively.

4. Results

4.1. Simulations

4.1.1. Continuous acquisition with rotational motion

Figure 4, shows the images that were reconstructed from $N = 40$ equally distributed motion blurred projections, which were simulated from the phantom in Fig. 2. The corresponding difference images in Fig. 4 show the difference between the phantom and the BBLS, ARTIC and RACE reconstruction. The normalized mean square error (NMSE) of the final BBLS, ARTIC and RACE reconstruction was 0.243, 0.094 and 0.033, respectively. The reconstructions from $N = 20$ and $N = 10$ are shown in Fig. 5 and Fig. 6, respectively, together with their corresponding difference images. Figure 7(a) shows the NMSE of the ARTIC and RACE reconstructions as a function of the number of iterations, for a set of $N = 10$, $N = 20$ and $N = 40$ equally distributed motion blurred projections, with a subsampling factor of $M = 120$, $M = 60$ and $M = 30$,

Optics EXPRESS

respectively. In Fig. 7(b), the NMSE of the ARTIC and RACE reconstructions is shown as a function of the number of iterations, for different levels of Poisson noise ($I_0 = 10^4$ and $I_0 = 10^5$).

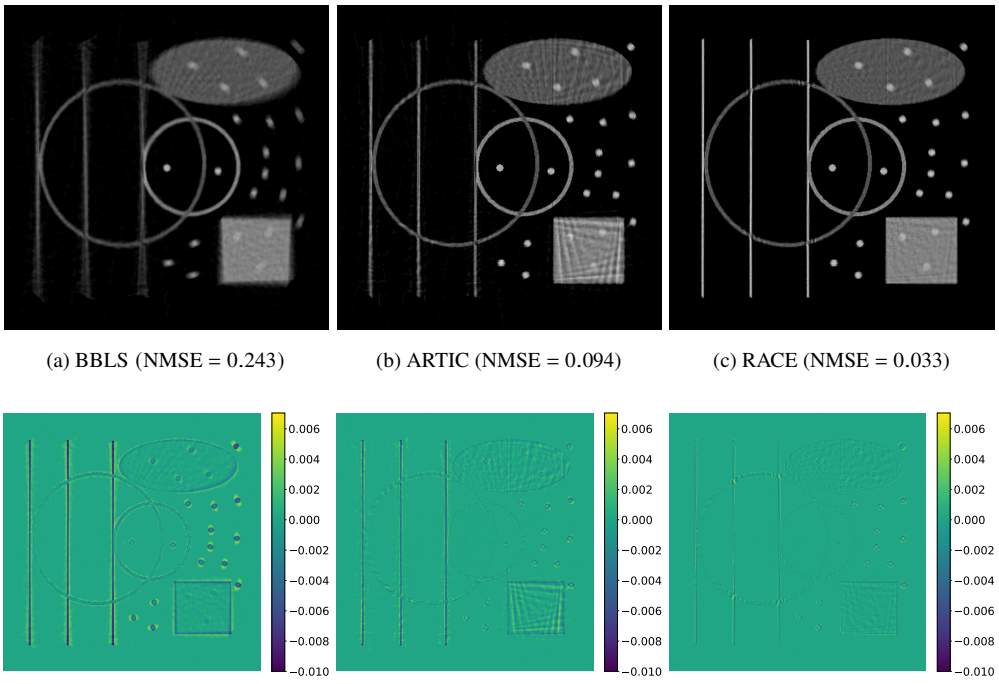

(a) BBLS (NMSE = 0.243) (b) ARTIC (NMSE = 0.094) (c) RACE (NMSE = 0.033)

(d) BBLS difference image (e) ARTIC difference image (f) RACE difference image

Fig. 4. BBLS, ARTIC and RACE reconstruction of the phantom and the corresponding difference images of the rotational simulation with $N = 40$ projections. For RACE and ARTIC a subsampling factor of $M = 30$ was used.

4.1.2. Continuous acquisition with both rotational and translational motion

Figure 8, Fig. 9 and Fig. 10 show the BBLS, ARTIC+ and RACE reconstructions of the phantom in Fig. 2 from $N = 10$, $N = 20$ and $N = 40$ equally distributed projections. The subsampling factors of ARTIC+ and RACE were $M = 120$, $M = 60$ and $M = 30$, respectively. Table 1 lists the reconstruction times of BBLS and RACE for the three simulated datasets.

Table 1. The approximate reconstruction times for BBLS and RACE for the three different simulated datasets with $N = 10$, $N = 20$ and $N = 40$ projections.

	Projections	Iterations	BBLS	RACE
Dataset 1	10	2000	152 s	458 s
Dataset 2	20	2000	161 s	456 s
Dataset 3	40	2000	155 s	432 s

4.2. Real measurements

Figure 11 shows the BBLS central slice reconstruction of the object depicted in Fig. 3(a). The image was reconstructed from a set of $N = 3600$ projections with negligible motion blur and serves as a reference image. Figure 12 shows the BBLS, ARTIC+ and RACE reconstructions from

Optics EXPRESS

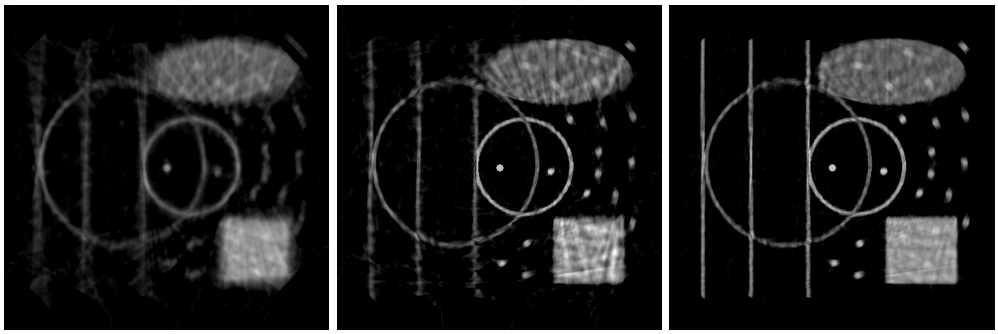

(a) BBLS (NMSE = 0.495) (b) ARTIC (NMSE = 0.264) (c) RACE (NMSE = 0.133)

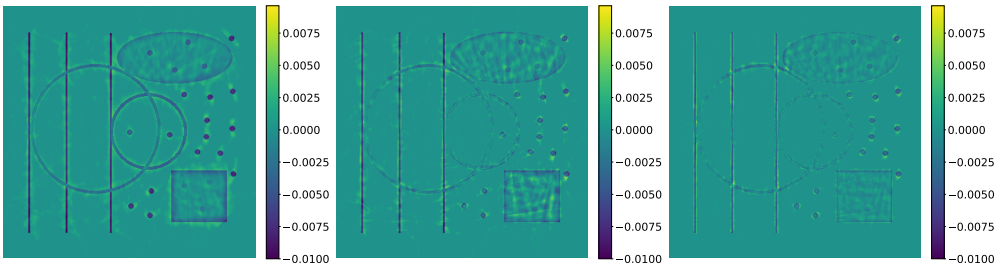

(d) BBLS difference image (e) ARTIC difference image (f) RACE difference image

Fig. 5. BBLS, ARTIC and RACE reconstruction of the phantom and the corresponding difference images of the rotational simulation with $N = 20$ projections. For RACE and ARTIC a subsampling factor of $M = 60$ was used.

a set of $N = 360$ motion blurred projections with a rotational blur of 1° and a translational blur of 0.48 mm. Similarly, Fig. 13 and Fig. 14 show the BBLS, ARTIC+ and RACE reconstructions from 180 and 90 motion blurred projections with a rotational blur of 2° and 4° and translation blur of 0.96 mm and 1.92 mm, respectively. Figure 15 shows the cross section through the upper horizontal edge of the top right block, as indicated in Fig. 11, for different amounts of motion blur. The reconstruction times of BBLS and RACE for the three datasets are shown in Table 2.

Table 2. The approximate reconstruction times for BBLS and RACE for the three different measured datasets with $N = 360$, $N = 180$ and $N = 90$ projections.

	Projections	Iterations	BBLS	RACE
Dataset 1	360	60	3 s	58 s
Dataset 2	180	70	2 s	66 s
Dataset 3	90	108	3 s	95 s

Optics EXPRESS

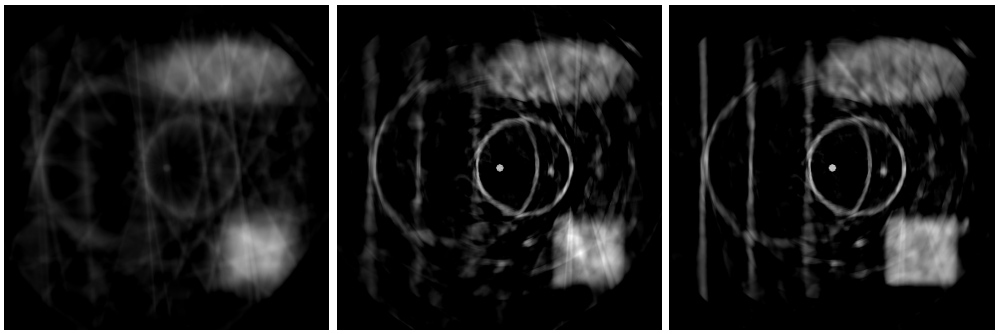

(a) BBLS (NMSE = 0.900) (b) ARTIC (NMSE = 0.498) (c) RACE (NMSE = 0.365)

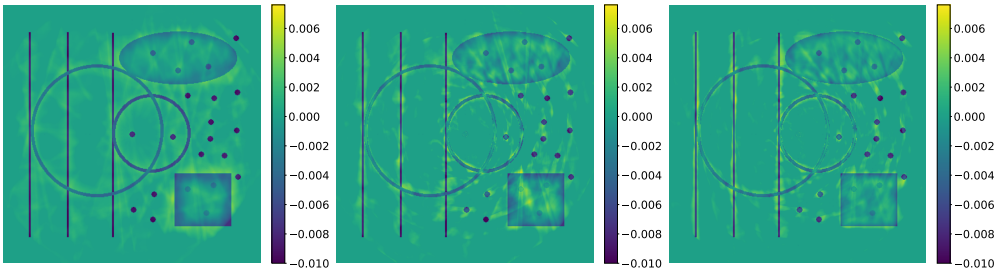

(d) BBLS difference image (e) ARTIC difference image (f) RACE difference image

Fig. 6. BBLS, ARTIC and RACE reconstruction of the phantom and the corresponding difference images of the rotational simulation with $N = 10$ projections. For RACE and ARTIC a subsampling factor of $M = 120$ was used.

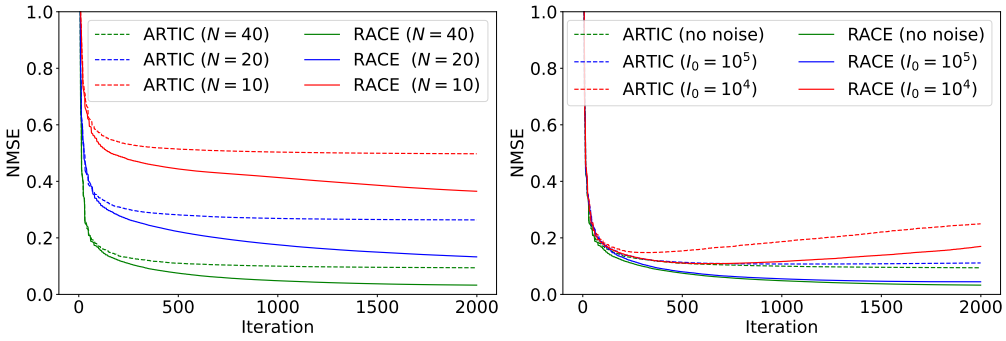

(a) NMSE for a different number of projections (b) NMSE for different Poisson noise levels

Fig. 7. The NMSE of the ARTIC and RACE reconstructions as a function of the iteration number, for a different number of projections (a) and for different noise levels with $N = 40$ projections (b).

Optics EXPRESS

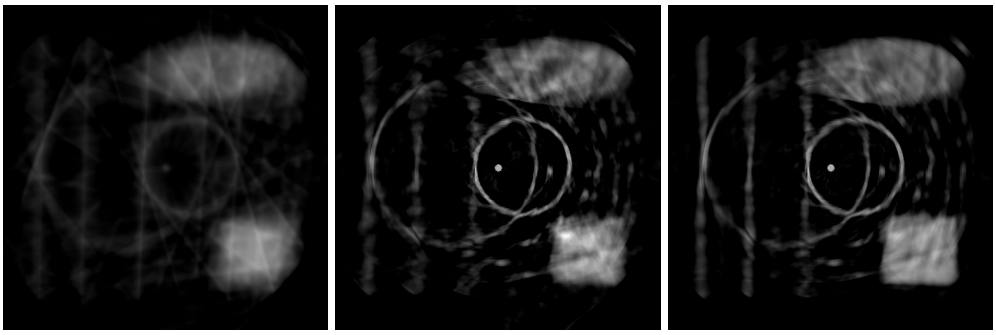

(a) BBLS (NMSE = 0.869) (b) ARTIC+ (NMSE = 0.482) (c) RACE (NMSE = 0.403)

Fig. 8. The BBLS, ARTIC+ and RACE reconstruction of the roto-translational simulation with $N = 10$ projections and a subsampling factor of $M = 120$.

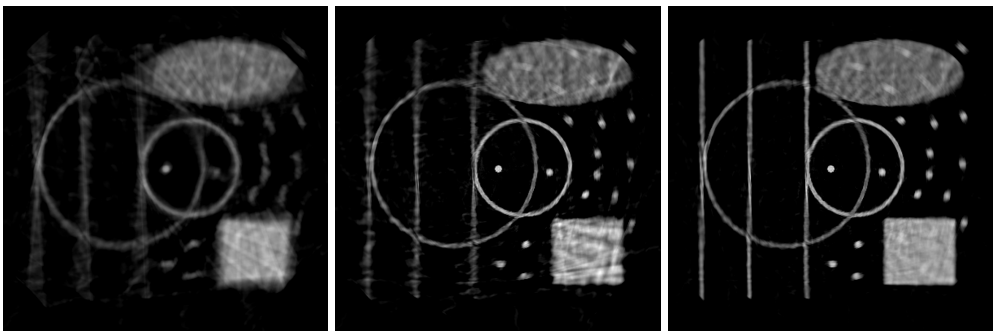

(a) BBLS (NMSE = 0.501) (b) ARTIC+ (NMSE = 0.269) (c) RACE (NMSE = 0.152)

Fig. 9. The BBLS, ARTIC+ and RACE reconstruction of the roto-translational simulation with $N = 20$ projections and a subsampling factor of $M = 60$.

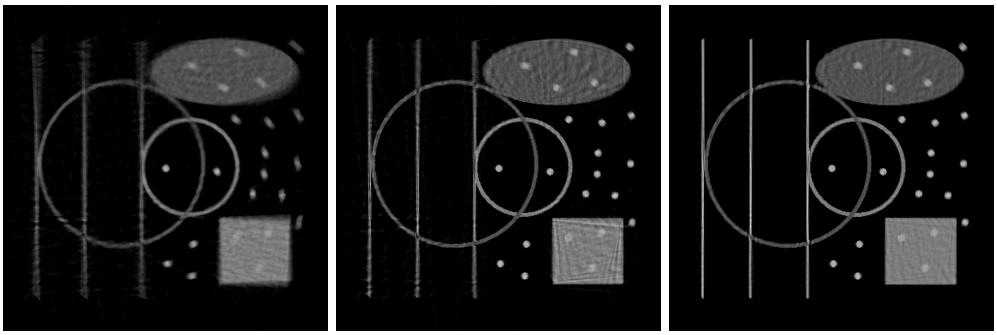

(a) BBLS (NMSE = 0.233) (b) ARTIC+ (NMSE = 0.109) (c) RACE (NMSE = 0.043)

Fig. 10. The BBLS, ARTIC+ and RACE reconstruction of the roto-translational simulation with $N = 40$ projections and a subsampling factor of $M = 30$.

Optics EXPRESS

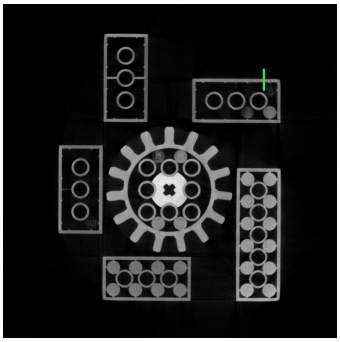

Fig. 11. Central slice reconstruction of the object in Fig. 3(a), from a set of $N = 3600$ projections with negligible motion blur. The vertical green line indicates the position of the cross sections shown in Fig. 15.

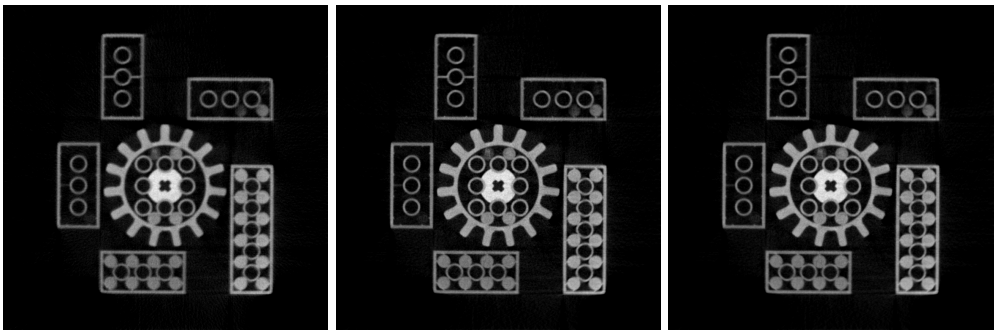

(a) BBLS (b) ARTIC+ (c) RACE

Fig. 12. The BBLS, ARTIC+ and RACE reconstruction for 360 projections with a rotational blur of 1° and a translational blur of 0.48 mm on the detector.

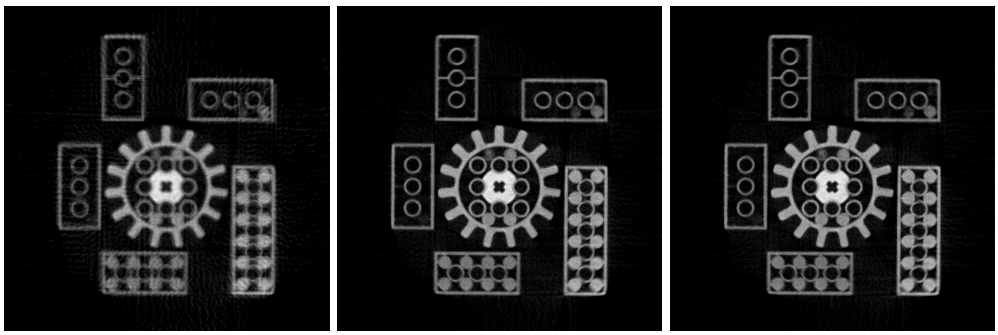

(a) BBLS (b) ARTIC+ (c) RACE

Fig. 13. The BBLS, ARTIC+ and RACE reconstruction for 180 projections with a rotational blur of 2° and a translational blur of 0.96 mm on the detector.

Optics EXPRESS

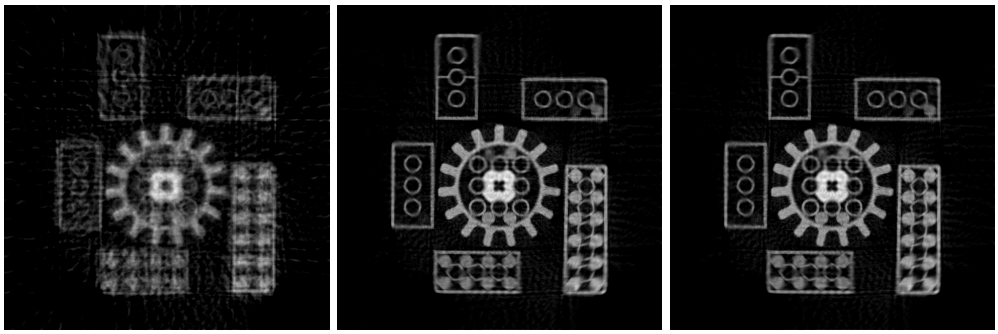

(a) BBLS (b) ARTIC+ (c) RACE

Fig. 14. The BBLS, ARTIC+ and RACE reconstruction for 90 projections with a rotational blur of 4° and a translational blur of 1.92 mm on the detector.

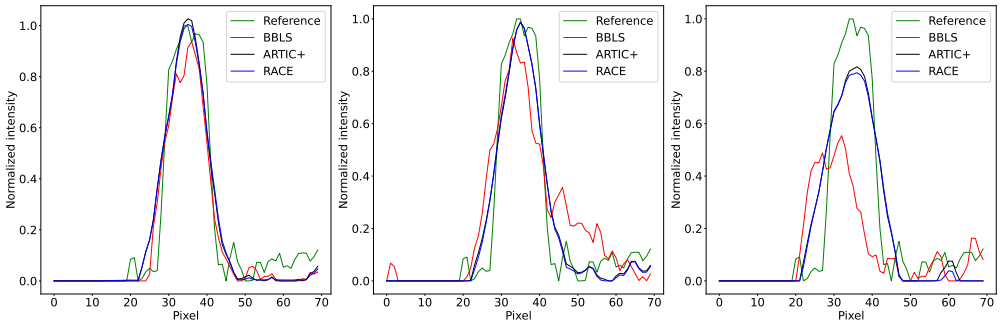

(a) Motion blur of 1° and 0.48 mm (b) Motion blur of 2° and 0.96 mm (c) Motion blur of 4° and 1.92 mm

Fig. 15. Cross section through the upper horizontal edge of the top right block (as indicated in Fig. 11) for different amounts of rotational and translational motion blur.

5. Discussion

5.1. Simulations

5.1.1. Continuous acquisition with rotational motion

The BBLS reconstruction, shown in Fig. 4(a), clearly shows motion artifacts corresponding to the continuous rotation during acquisition. The random dots are smeared out tangentially and the vertical lines are also smeared out towards the ends. However, the central dot is not visibly blurred because it is invariant under rotation. The ARTIC reconstruction in Fig. 4(b) shows a clear reduction of motion artifacts. Most dots, vertical lines and edges are now sharper and less smeared out. However, the structures farthest away from the center are still visibly blurry and although the vertical lines are sharper defined, they now exhibit darker and brighter streaks. The RACE reconstruction in Fig. 4(c) shows an improvement in reconstruction quality compared to the ARTIC reconstruction. Most notably, the vertical lines are now sharply defined and most of the bright and dark streaks in the lines are removed. The improvement in reconstruction quality can also be visualized by the difference images, shown in Fig. 4, where the difference between the phantom and the respective reconstruction is shown. Additionally, the phantom was reconstructed from $N = 20$ and $N = 10$ equally distributed projections and the reconstructions are shown in Fig. 5 and Fig. 6. Results show that also for a lower number of projections RACE outperforms ARTIC in terms of reconstruction quality. The NMSE of the ARTIC and RACE

Optics EXPRESS

reconstructions is plotted in Fig. 7(a) as a function of the iteration number, where it shows that RACE converges to a smaller NMSE than ARTIC, and it does so at a faster rate.

In a final experiment, different amounts of Poisson noise were added to the simulated projections. In Fig. 7(b), the NMSE of the ARTIC and RACE reconstructions are plotted. The figure shows that, independent of the noise level, RACE performs better than ARTIC in terms of the NMSE.

5.1.2. Continuous acquisition with both rotational and translational motion

The phantom in Fig. 2 was reconstructed with BBLS, RACE and ARTIC+ to compare the reconstructions. First, only 10 projections were used, resulting in the reconstructions shown in Fig. 8. Here, it can be observed that the BBLS reconstruction quality suffers heavily from the limited data and high amount of rotational blurring of 19.4° per projection. The ARTIC+ reconstruction has an improved reconstruction quality, but still heavily suffers from streaking artifacts. In the RACE reconstruction, the streaking artifacts are slightly less apparent and the vertical lines are more clearly defined compared to the ARTIC+ reconstruction.

Next, a reconstruction with 20 projections was performed, shown in Fig. 9. The BBLS reconstruction quality improved compared to the reconstruction with 10 projections in Fig. 8. However, the vertical lines and dots are still not distinguishable. The ARTIC+ reconstruction is considerably better compared to the BBLS reconstruction. The vertical lines and dots are distinguishable, although still blurry. In contrast, the RACE reconstruction shown in Fig. 9(c) clearly shows sharper vertical lines and dots. Also, the edges of the square and ellipse are much more sharply defined. However, there are still visible blurring artifacts, especially for the structures farthest from the center.

Finally, a BBLS, ARTIC+ and RACE reconstruction were performed with 40 projections, shown in Fig. 10. While the BBLS reconstruction quality improved and the vertical lines and dots are now distinguishable, the blurring artifacts are still apparent. In the ARTIC+ reconstruction the vertical lines, edges and dots are more sharp, but some artifacts remain in the form of streaks through the structures. In the RACE reconstruction, these streaks are greatly reduced, resulting in an even higher image quality. Only the most outward structures still show a small amount of blurring.

While RACE considerably improves the reconstruction quality compared to BBLS, the downside is that it is more computationally expensive due to the subsampling. For the three datasets of $N = 10$, $N = 20$ and $N = 40$ projections, the BBLS and RACE reconstruction times are listed in Table 1. Here, it can be seen that the RACE reconstruction takes almost three times as long as the BBLS reconstruction. For a 2D reconstruction of a slice, this time increase might be of less importance. However, when performing a 3D reconstruction, this can be limiting. Therefore, one must consider the advantage of reduced blurring against the disadvantage of increased reconstruction time. Alternatively, the subsampling factor can be reduced to below the recommended value, as calculated by Eq. (3) to optimize both the reconstruction quality and reconstruction time.

5.2. Real measurements

First, a BBLS, ARTIC+ and RACE reconstruction were performed on a data set of 360 motion blurred projections, with approximately 1° of rotational blur and 0.48 mm of translational bur per projection. The resulting images are shown in Fig. 12. For this amount of motion blur, it is difficult to see blurring artifacts. The cross sections in Fig. 15(a) are also of similar width, indicating that the edges are not strongly smeared out due to the motion.

Then, BBLS, ARTIC+ and RACE were performed on a set of 180 motion blurred projections, with 2° of rotational blur and 0.96 mm of translational bur per projection. The reconstructions are shown in Fig. 13. In the BBLS reconstruction, blurring artifacts are visible in the form of double edges on the blocks and smaller details that are not visible anymore, like the protrusions

Optics EXPRESS

on the edges on the inside of the blocks. In the ARTIC+ and RACE reconstruction, the edges are more clearly defined, as also demonstrated by the cross section shown in Fig. 15(b). The cross section of the edge in the BBLS reconstruction is smeared out, while the cross section through the edge in the ARTIC+ and RACE reconstruction matches the reference line well. A secondary effect that causes image quality degradation is the smaller number of projections, which is fixed by the total angular range divided by the angle rotated during acquisition of one projection. Therefore, the maximal number of projections with a 2° of rotational blurring in one rotation of the object is 180.

Finally, a dataset of 90 motion blurred projections with a rotational blur of 4° and translational blur of 1.92 mm was reconstructed with BBLS, ARTIC+ and RACE. The reconstructions are shown in Fig. 14. The edges of the blocks in the BBLS reconstruction are now severely blurred and the entire image suffers from many artifacts, compared to the ARTIC+ and RACE reconstruction. This is also reflected in the cross sections shown in Fig. 15(c), where the line of the BBLS reconstruction is largely smeared out and low in intensity. The cross section of the line in the ARTIC+ and RACE reconstruction is now also visually broader, but still recognizable as a line profile.

For the real experiments, the performance of RACE seems comparable to that of ARTIC+. This may be due to the smaller amount of blurring and larger number of projections in the experimental data compared to the simulated data, where a clear improvement of RACE over ARTIC and ARTIC+ can be seen. Figure 7(a) also shows that for an increasing number of projections (and thus decreasing amount of blur) the NMSE of ARTIC and RACE approach each other. We note that, comparing both reconstructions quantitatively is challenging because of the absence of a true ground truth image [26]. Finally, since RACE requires a non-linear optimization technique, its computational complexity is higher than that of ARTIC which relies on a linear solver for image reconstruction. The approximate reconstruction times of BBLS and RACE are listed in Table 2.

In Section 2, we derived the equations for monochromatic X-rays. Extension to a polychromatic spectrum can be done by integrating Eq. (1) over the X-ray spectrum. However, this does not interfere with the subsampling approach of RACE. We also assumed a constant object speed throughout the scan. Although, some applications might require to model object acceleration. Future work includes adapting the subsampling scheme in RACE to also accommodate for acceleration. Now, the time interval over which the intensity is integrated was divided into M parts of equal length, which gives the same weight to each subsampled interval. This is a valid approach for objects moving at a constant speed. However, when the object accelerates or decelerates, this is no longer valid. As such, acceleration of the object can be included by dividing the integration interval into non-equal parts. Future work also includes the addition of regularization, for example based on total variation minimization or by employing a deep image prior network for regularization [27]. Also, in this work the motion of the object was assumed to be known, which allowed us to calculate the subsampling prior to the reconstruction. Object motion can however also be estimated during the reconstruction process, as for example shown in [28]. Finally, because this research is also valuable for application in synchrotrons, we created separate code to validate ARTIC and RACE for a parallel beam geometry, openly available at [29].

6. Conclusion

RACE was proposed to reconstruct images based on a set of motion blurred projections acquired during an X-ray scan with continuous acquisition. It is applicable to scans with rotational motion as well as scans that combine rotational and translational motion, because it allows for a generalized model of motion during X-ray exposure. We demonstrated the potential of RACE in reconstructing motion blurred projections obtained by both simulations and experiments. We

Optics EXPRESS

showed that RACE results in reduced motion blur artifacts and a higher reconstruction quality, compared to BBLS and ARTIC, especially for scans with limited data acquisition and a high amount of blurring. Future work includes the modeling of object acceleration and deceleration by adapting the subsampling scheme used by RACE.

Funding. Fonds Wetenschappelijk Onderzoek (1S46122N, 1SA2920N, G090020N, G094320N).

Disclosures. The authors declare that there are no conflicts of interest related to this article.

Data availability. The code and data from this study are available at [29] and [30], respectively.

References

1. W. A. Kalender, "X-ray computed tomography," Phys. Med. Biol. **51**(13), R29–R43 (2006).
2. H. U. Kerl, C. T. Isaza, H. Boll, *et al.*, "Evaluation of a continuous-rotation, high-speed scanning protocol for micro-computed tomography," J. Comput. Assist. Tomogr. **35**(4), 517–523 (2011).
3. X. Guo, S. M. Johnston, Y. Qi, *et al.*, "4D micro-CT using fast prospective gating," Phys. Med. Biol. **57**(1), 257–271 (2012).
4. J. Renders, J. Sijbers, and J. De Beenhouwer, "Adjoint image warping using multivariate splines with application to four-dimensional computed tomography," Med. Phys. **48**(10), 6362–6374 (2021).
5. E. A. Zwanenburg, M. A. Williams, and J. M. Warnett, "Review of high-speed imaging with lab-based x-ray computed tomography," Meas. Sci. Technol. **33**(1), 012003 (2022).
6. T. De Schryver, J. Dhaene, M. Dierick, *et al.*, "In-line NDT with X-ray CT combining sample rotation and translation," NDT & E International **84**, 89–98 (2016).
7. J. M. Warnett, V. Titarenko, E. Kiraci, *et al.*, "Towards in-process x-ray CT for dimensional metrology," Meas. Sci. Technol. **27**(3), 035401 (2016).
8. O. Brunke, F. Hansen, I. Stuke, *et al.*, "A new concept for high-speed atline and inlineCT for up to 100% mass production process control allowing both, 3D metrology and failure analysis," in *4th Conference on Industrial Computed Tomography (iCT)*, (2012), pp. 385–391.
9. W. A. Kalender, "Technical foundations of spiral CT," Semin. Ultrasound CT MRI **15**(2), 81–89 (1994).
10. J. Cant, G. Behiels, and J. Sijbers, "Continuous digital laminography," in *6th Conference on Industrial Computed Tomography (iCT)*, (2016), pp. 1–5.
11. D. Vavřík, J. Jakůbek, I. Kumpova, *et al.*, "Laboratory based study of dynamical processes by 4D X-ray CT with sub-second temporal resolution," J. Inst. **12**(02), C02010 (2017).
12. J. Zheng, J. A. Fessler, and H.-P. Chan, "Effect of source blur on digital breast tomosynthesis reconstruction," Med. Phys. **46**(12), 5572–5592 (2019).
13. C. Lee and J. Baek, "Effect of optical blurring of X-ray source on breast tomosynthesis image quality: Modulation transfer function, anatomical noise power spectrum, and signal detectability perspectives," PLoS One **17**(5), e0267850 (2022).
14. J. Cant, W. J. Palenstijn, G. Behiels, *et al.*, "Modeling blurring effects due to continuous gantry rotation: Application to region of interest tomography," Med. Phys. **42**(5), 2709–2717 (2015).
15. D. Chen, H. Li, Q. Wang, *et al.*, "Computed tomography for high-speed rotation object," Opt. Express **23**(10), 13423–13442 (2015).
16. J. Zhang, W.-K. Lee, and M. Ge, "Sub-10 second fly-scan nano-tomography using machine learning," Commun. Mater. **3**(1), 91 (2022).
17. S. Majee, S. Aslan, D. Gürsoy, *et al.*, "CodEx: A Modular Framework for Joint Temporal De-Blurring and Tomographic Reconstruction," IEEE Trans. Comput. Imaging **8**, 666–678 (2022).
18. E. Maire, J.-Y. Buffière, L. Salvo, *et al.*, "On the application of x-ray microtomography in the field of materials science," Adv. Eng. Mater. **3**(8), 539–546 (2001).
19. H. Hiriyannaiah, "X-ray computed tomography for medical imaging," IEEE Signal Process. Mag. **14**(2), 42–59 (1997).
20. J. Barzilai and J. M. Borwein, "Two-point step size gradient methods," IMA J. Numer Anal. **8**(1), 141–148 (1988).
21. W. van Aarle, W. J. Palenstijn, J. Cant, *et al.*, "Fast and flexible X-ray tomography using the ASTRA toolbox," Opt. Express **24**(22), 25129–25147 (2016).
22. D. L. Parker, "Optimal short scan convolution reconstruction for fanbeam CT," Med. Phys. **9**(2), 254–257 (1982).
23. C. Boncelet, *The Essential Guide to Image Processing* (Academic Press, 2009), chap. 7, pp. 143–167.
24. B. De Samber, J. Renders, T. Elberfeld, *et al.*, "FleXCT: a flexible X-ray CT scanner with 10 degrees of freedom," Opt. Express **29**(3), 3438–3457 (2021).
25. University of Antwerp, "DynXLab: center for 4D Quantitative X-ray Imaging and Analysis," https://www.uantwerpen.be/dynxlab. Last accessed 30 May 2024.
26. J. Wang, D. An, and J. P. Haldar, "The "hidden noise" problem in MR image reconstruction," Magnetic Resonance in Med. **92**(3), 982–996 (2024).
27. D. Ulyanov, A. Vedaldi, and V. Lempitsky, "Deep image prior," Int. J. Comput. Vis. **128**(7), 1867–1888 (2020).
28. V. Van Nieuwenhove, J. De Beenhouwer, T. De Schryver, *et al.*, "Data-driven affine deformation estimation and correction in cone beam computed tomography," IEEE Trans. on Image Process. **26**(3), 1441–1451 (2017).
29. B. Huyge, "RACE," https://github.com/BenHuyge/RACE (2024). Last accessed 31 June 2024.
30. B. Huyge, J. Renders, J. Sanctorum, *et al.*, "X-ray image reconstruction for continuous acquisitions with a universal motion model: Data," https://doi.org/10.5281/zenodo.12918504 (2024). Last accessed 31 June 2024.